Hindawi
Structural Control and Health Monitoring
Volume 2023, Article ID 6932621, 19 pages
https://doi.org/10.1155/2023/6932621

Research Article

Permanent Deformation Monitoring and Remaining Life Prediction of Asphalt Pavement Combining Full-Scale Accelerated Pavement Testing and FEM

Zhen Liu, Xingyu Gu, Hua Ren, Shuwei Li, and Qiao Dong

Department of Roadway Engineering, School of Transportation, Southeast University, Nanjing 211189, China

Correspondence should be addressed to Xingyu Gu; 230208344@seu.edu.cn

Received 10 December 2022; Revised 12 May 2023; Accepted 19 May 2023; Published 8 June 2023

Academic Editor: Łukasz Jankowski

Permanent deformation (rutting) is one of the typical failure modes of asphalt pavement with a semirigid base in high-temperature areas. To address issues of pavement structure deformation and remaining life prediction, a method of combining accelerated pavement testing and finite element (FE) simulation was proposed. A modified Burgers model considering creep parameter damage was obtained using strain monitoring data and laboratory test values, which was performed in the FE model to analyze rutting development. The results showed that high temperature and heavy axle loads greatly influenced rutting development: the tested road was loaded 360,000 times at high temperature, contributing 50% to accumulated rutting; rutting increased by 90.7% under the condition of 50% overload under high-temperature seasons from the simulated results. Then, the ratio of the bulge area to the depression area (K_R) was proposed to define the rutting deformation mechanism. The K_R analysis results illustrated that rutting development was a transition process from compaction rutting to flow rutting. Finally, the relationship between the action times of axle load in the tested and in-service roads was established based on the rutting equivalence principle. When the action times of axle load reach approximately 25 million times (insufficient remaining life) for the investigated Hu-Ning highway, necessary maintenance measures should be taken to treat rutting deformation.

1. Introduction

Asphalt pavement is the main pavement form of high-grade highways in China [1–6]. Rutting, one of the typical failure modes of asphalt pavement with a semirigid base in high-temperature areas, seriously damages the pavement quality and durability and affects driving safety and comfort [7–11]. Therefore, improving the accuracy and universality of rutting estimation is crucial and effectively preventing and treating the asphalt pavement [12, 13]. For the rutting development law of asphalt pavement, researchers divided the process into three stages [14]: (1) the first stage is the initial compaction period: the asphalt mixture is compressed rapidly under vehicle loading. Rutting deformation shows a short-term rapid accumulation. (2) The second stage is the continuous development period: the resistance to deformation of the asphalt mixture increases gradually, resulting in a consolidation effect. The deformation rate of rutting decreases rapidly and tends to be stable. (3) The third stage is the accelerated deformation period: the skeleton interaction in pavement has been destroyed under repeated loads. The pavement structure experiences shear flow failure under shear stress.

Currently, there are three representative approaches for rutting prediction: the first is the theoretical method, which establishes the relationship between the mechanical parameters and the permanent deformation of the pavement structure based on mechanical hypotheses. Representative models were the SHELL rutting prediction model considering dynamic correction [15] and the A. Wijeratne model [16]. Using the stress-strain

relationship, rutting can be predicted using the stresses of different layers and point positions along the road structure [17]. Unfortunately, the accuracy of these models is highly dependent on mechanical assumptions and material parameters, and the parameters obtained from laboratory tests are quite different from the actual conditions. This has become the main limitations in rutting prediction using the theoretical method.

The second is the empirical method that finds the relationship between rutting deformation and its impact factors using statistical means to construct the regression equation. By incorporating the measured rutting data, it is able to obtain the rutting calculation equation with various model parameters. Shami et al. [18] proposed an exponential prediction model based on the number of shaft loads and temperature through indoor tests. Archilla and Madanat [19] proposed a prediction model considering road characteristics and load times based on the AASHTO test data. Based on indoor test and accelerated loading tests, Zhenglan and Lijun [20] obtained rutting curves of different working conditions and structures respectively, and established the prediction model considering the shear strength, shear stress, loading times, road temperature, and driving speed, etc. However, these models are only established based on the statistical data of specific pavement structures and there is no specific explanation of the performance changes of asphalt mixtures during the rutting process. Thus, it has limitations and a small range of application.

The third is the mechanistic-empirical method [21, 22], which is the Mechanistic-Empirical Pavement Design Guide (MEPDG). Based on this method, the rutting prediction model is mainly developed using the measured data and asphalt pavement state in actual use. The rutting prediction model obtained by this method is more in line with the actual situation and many scholars have discussed it. Gulfam et al. developed a calibration database for rutting and roughness data, which reduced the prediction error of rutting by MEPDG software [23]. Abdelfattah et al. [24] combined rutting testing data and numerical simulation results to verify, calibrate, and validate MEPDG rutting models. Results proved that this approach for calibrating the MEPDG rutting models was worth promoting. Zhu et al. [25] considered the deformation of structural layer of asphalt surface and obtained the final rutting by superposition. The temperature of asphalt layer, the number of axial loads, load velocity and shear stress were introduced into the model, and the prediction model was obtained by combining with the measured data. However, the pavement structure layer in this study was relatively simple, which is difficult to represent the typical semirigid base pavement. The main difficulty of this method is that the calculation process of permanent deformation contains many empirical fitting parameters and experimental mechanical parameters that need long-term tracking and observation to verify the accuracy of rutting prediction model [26].

As for the acquisition method of rutting performance, traditional laboratory tests [27, 28], accelerated pavement testing (APT) [29], and field observations on roads [30] are mainly used. APT can better simulate vehicle load action [31–33] and obtain the actual road surface performance under long-term driving load action in the short-term [34, 35]. Thus, it has been widely used in road engineering for research on rutting resistance, formation, and prediction of asphalt pavement. Zhou and Scullion [36] used a VESYS5 computer program to correlate with existing APT data and wrote a model program to determine the rutting coefficient, depth, and damage. Hugo et al. [37] utilized APT equipment to carry out several loading tests and established rutting prediction models. However, using APT equipment was associated with high costs [38, 39]. Furthermore, the research conclusions have limited guiding effects on actual pavements due to the limitation of axle load and speed of APT equipment [40, 41]. Altogether, the role of APT for rutting prediction is limited. Recently, prediction rutting using numerical simulations is getting more popular [42–44]. Among them, finite element (FE) analysis is one of the most effective methods [45]. The FE method could make up for the deficiency of short-term APT tests and conduct comprehensive mechanical response analysis of pavement structure, while its prediction accuracy is always needed to be improved.

Overall, the key to rutting prediction is obtaining accurate external parameters and the mechanical parameters of the mixture during the service period. Load and environmental parameters can be acquired at the APT site, but the material parameters obtained in the laboratory test often deviate from the actual pavement structure parameters. More analyses and correlation transformations between laboratory tests and APT should be conducted. Therefore, this paper aims to compare the parameter difference between laboratory tests and actual pavement structures based on previous rutting prediction research by the MEPDG method. The innovative points of this study are as follows: (1) a rutting prediction model reflecting real pavement parameters is established; (2) the ratio of the bulge area to the depression area (K_R) is proposed to define the rutting deformation mechanism; and (3) the relationship between the action times of axle load in the tested and in-service roads is established based on the rutting equivalence principle. These innovations could provide a scientific reference for the rutting treatment and maintenance of asphalt pavement with a semirigid base.

2. Objective

This paper analyzes the rutting development and evolution rules of asphalt pavement based on APT. Several objectives are drawn as follows:

(1) To analyze the rutting evolution law in depth from three aspects: rutting section morphology, rutting development law, and rutting deformation mechanism.

(2) To establish the FE model with more precise parameters and verify the reliability with rutting monitoring data in the full-scale APT and actual road in service.

(3) To predict the permanent deformation of actual road structures under different working conditions and propose a reasonable maintenance time.

For this purpose, some indoor tests were conducted, including material parameter tests, repeated loading tests, and dynamic creep tests. Full-scale APT with MLS66 and FE modeling with the modified Burgers model were also performed.

3. Methodology

3.1. Experiment Design

3.1.1. Field Pavement Testing. The typical pavement structure of asphalt pavement with semibase was studied in Jiangsu Province, China [41]. For the asphalt surface layer, basalt and SBS-modified asphalt were used at the SMA-13 layer with an asphalt-aggregate ratio of 6.0%; limestone and SBS-modified asphalt were used at the SUP-20 layer with an asphalt-aggregate ratio of 4.3%; limestone and $70^{\#}$ base asphalt were used at the SUP-25 layer with an asphalt-aggregate ratio of 4.0%. For the base layer, CSM with 4.3% cement was used at the upper and lower base layers; CSM with 3.0% cement was used at the subbase layer. Moreover, lime-ash soil (LAS) was used at the subgrade layer. Table 1 gives the performance test results of these materials; all the test indexes meet the specification requirements.

According to the test specification of pavement (JTG 3450-2019) of China industry, four rutting sections were selected in the loading band of the test section and measured in real-time using a self-rutting section recorder, as described in Figure 1 [46]. The loading scheme was as follows: loading one million times with an axle load of 50 kN and speed of 22 km/h.

Considering that the steel pieces used to place the rut section instrument at both ends would be loosened due to artificial or other external factors, the rutting data within the range of 0 mm to 1200 mm were corrected by the linear interpolation method in the data processing process. Thus, the deformation at the beginning and end of the rutting curve was zero. To analyze the deformation of the section in different structural layers of the test track, the section producing rutting in the test track was cut, and the deformation of each layer was measured after all the loading was completed. Besides, pavement rutting deformation was divided into two parts:

(1) One was the vertical stress affected loading weight area (mainly compaction deformation). The surface shape change was depression, and its area was denoted as S_D.

(2) The second was the shear stress affected area of the loading weight edge (mainly flow deformation). The surface shape change was a bulge, and its area was denoted as S_B.

As shown in Figure 2, the ratio of S_B and S_D at the rutting section, K_R, was defined as the index to judge the cause of rutting deformation, as shown in (1).

$$K_R = \frac{S_B}{S_D},$$
$$S_B = S_1 + S_3 + S_5, \quad (1)$$
$$S_D = S_2 + S_4,$$

where K_R increases and decreases with increasing loading times, it indicates that rutting deformation is mainly flow deformation and compaction deformation, respectively. When K_R remains constant, the rutting deformation coincides with compaction and flow deformation.

The elevation difference between the highest point and lowest point of the rutting section was defined as the rutting deformation amount to study the change in rutting with loading times, temperature, and other influencing factors. The temperature was represented by the real-time temperature collected by the middle surface layer sensor in the test road.

3.1.2. Sensor Monitoring Scheme. Figure 3 describes the sensor monitoring scheme of different pavement structural layers. The selection and reliability verification of sensors have been mentioned in previous studies [46–48]. Under the center of the wheel track, longitudinal, lateral, and vertical asphalt strain gauges were embedded in the middle and bottom asphalt surface layers [49, 50]. Longitudinal and lateral concrete strain gauges were embedded in the bottom of the base layer. The earth manometer was embedded in the top surface of the base and the subgrade layers. In addition, two to three temperature sensors were buried at the edge of each layer, and the humidity sensors were mainly buried in the bottom base and subgrade layers.

Six groups of monitoring data, including vertical, longitudinal, and lateral strains of the middle and bottom asphalt surface layers, were used for the structural parameter inversion.

3.1.3. Laboratory Test. Dynamic modulus test was conducted for the six core samples from the unloaded section and loaded section (after one million times), according to the China Industry standards (JTG E20-2011). The test methods and parameters are described in Reference [51].

A repeated loading test was performed using UTM-25 to fatigue the damaging effect of the dynamic modulus. Wheel pressure was set as 0.7 MPa, and the test temperature was set as 40°C, 50°C, and 60°C, respectively. The residual dynamic modulus of the specimen was tested at each loading time of 900 times. The residual dynamic modulus under different loading times was obtained through repeated loading tests of 1800 times, 2700 times, 3600 times, 4500 times, and 5400

Table 1: Performance test results of road materials at different structural layers.

Structural layers		Mean dynamic stability (time/mm)	Residual stability (%)	Freeze thaw splitting tensile strength ratio (%)	Bending failure strain ($\mu\varepsilon$)
Asphalt surface	SMA-13	5550	89.1	83.2	2613
	SUP-20	5284	90.6	79.9	2128
	SUP-25	3452	87.1	84.2	2731
Structural layers		Maximum dry density (g/cm^3)	Optimum moisture content (%)	Strength (MPa)	Ash content (%)
Base	CMS1	2.356	4.3	4.38	—
Subbase	CMS2	2.323	3.7	3.48	—
Subgrade	LAS	1.817	16.7	—	6.1

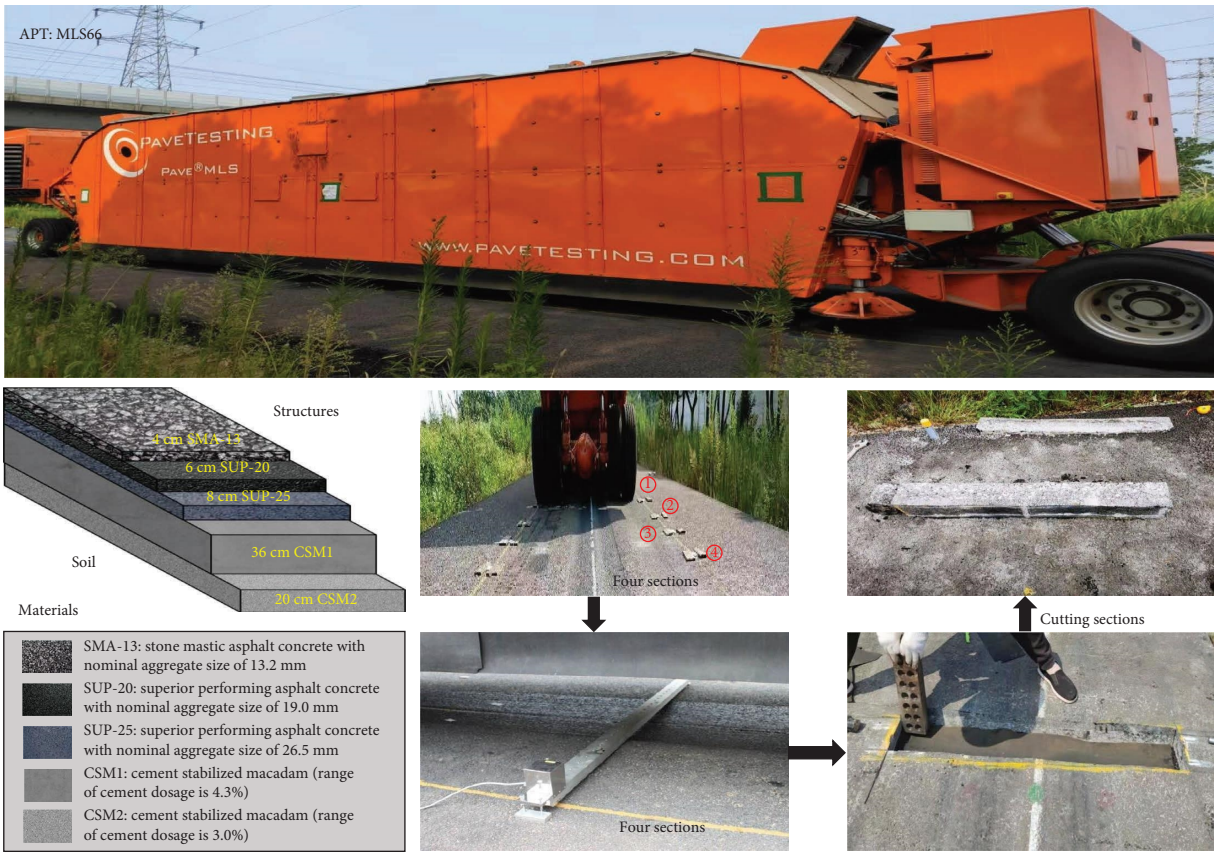

Figure 1: Diagram of road structures, rutting measurement, and accelerated pavement tests.

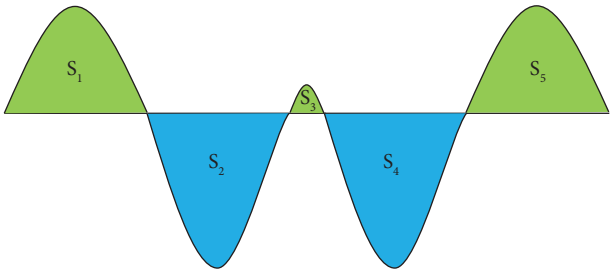

Figure 2: Diagram for the area of the bulge and depression parts.

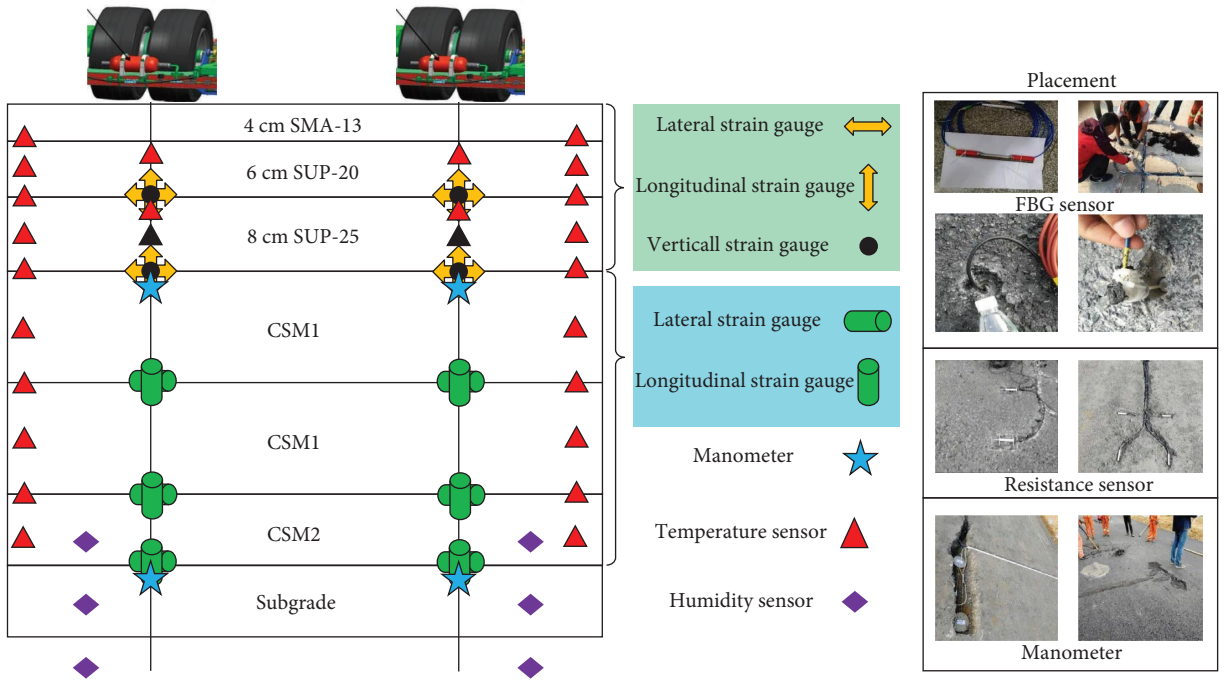

Figure 3: Sensor placement and monitoring schemes of pavement structures.

times. The test results were transformed and fitted according to (2) to establish the relationship between damage and loading time (t).

$$E = E_0(1 - \omega), \tag{2}$$

where E and E_0 are the material performance parameters at the initial and damaged states, respectively, and ω is the damage value.

Dynamic creep test was also designed to obtain accurate parameters for subsequent rutting estimation. Specimens with a diameter of 150 mm and a height of 180 mm were obtained from the test road. Dynamic creep tests were carried out at 40°C, 50°C, and 60°C using a UTM-25 machine. Before the test, the specimens were kept warm for more than four hours in a temperature control box. During the test, the axial loading force was set as 700 kPa, and the contact pressure was set as 20 kPa. The test will terminate when the vertical accumulative strain reaches 10,000 $\mu\varepsilon$ or repeated loading reaches 20,000 times.

3.2. Simulation Design

3.2.1. Constitutive Model. In previous studies [47, 51], the damaging effect of material parameters with loading times was considered in the creep strain $\varepsilon(t)$. The modified Burgers model was obtained in (3) by studying the attenuation law of the dynamic modulus under repeated loading.

$$\varepsilon(t) = \sigma_0\left[\frac{1}{E_0(1-\omega)} + \frac{1}{E_2}\left(1 - e^{-(E_2/\eta_2)t}\right) + \frac{1}{A}e^{Bt}\right], \tag{3}$$

where E_2 is the internal damper parameter. A, B, and η_2 are the fitted parameters. Unfortunately, this model only corrects the damage to the external spring's elastic coefficient and does not consider the damaging effect of the asphalt mixture in the whole creep process. The elastic deformation will recover with the unloading of the load and cannot be reflected in the permanent road deformation. Therefore, the damage of E_2, η_2, and A of the inner adhesive pot was considered based on (3) to establish the new damage equation in (4).

$$\varepsilon(t) = \frac{\sigma_0}{1-\omega}\left[\frac{1}{E_1} + \frac{1}{E_2}\left(1 - e^{-(E_2/\eta_2)t}\right) + \frac{1}{A}e^{Bt}\right]. \tag{4}$$

As described in Figure 4, the load was simplified as a rectangular uniformly distributed load to avoid the problem of nonconvergence and singularities caused by the circular loading model. Then, the dynamic load σ was equivalent to the static load σ_0 by using the principle of stress impulse equivalence for simulating rutting deformation, as shown in (5). Load parameters for the rutting simulation model were the same as in Reference [51].

$$\sigma_0 = \frac{2}{\pi}\sigma. \tag{5}$$

3.2.2. Material Parameters. According to the results in Section 4.2.1, the full-scale test track's dynamic modulus was only 62% of the initial state after loading one million times. Therefore, relevant results of laboratory tests cannot be directly applied to full-scale tests. The damage evolution

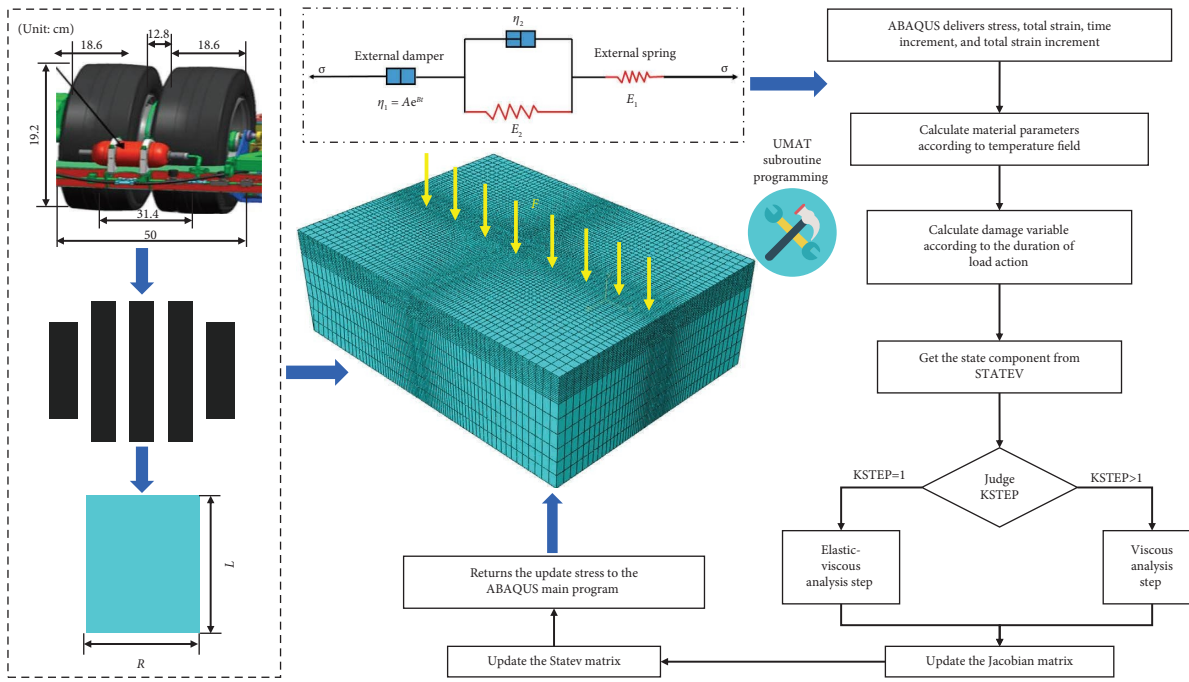

Figure 4: Diagram of the loading simplification, constitutive model, UMAT subroutine, and FE model.

equation in Figure 5(b) was transformed in the following steps:

(1) According to Figure 5(a), the loading time with a modulus damage value of 38% at different temperatures was calculated.

(2) The loading time with a modulus damage value of 38% was defined as the cumulative loading time for one million loading times.

(3) The data at other time points were transformed to the same scale, and the dynamic modulus equation and damage evolution equation were fitted again, as shown in (6).

$$\begin{aligned} \omega &= 0.000412t^{0.656}, temperature = 40^{\circ}C, \\ \omega &= 0.000465t^{0.641}, temperature = 50^{\circ}C, \\ \omega &= 0.000183t^{0.511}, temperature = 60^{\circ}C. \end{aligned} \tag{6}$$

In addition, the asphalt surface modulus (E_1) in the FM model at different temperatures was set based on the test results in Figure 5. Six types of monitoring data were obtained in the FE model for different moduli. The error S between the measured strains ε_M and the simulated strains ε_S was obtained according to (7). When the error was less than 5%, the simulation stopped, and E_1 was used as the input parameter of the FE model in Table 1.

$$S = \sqrt{\frac{1}{6}\sum_{i=1}^{6}\left|\frac{\varepsilon_M - \varepsilon_S}{\varepsilon_M}\right|}. \tag{7}$$

Then, the experimental results in Figure 5 were used to fit (4). Other creep parameters of asphalt mixtures at different temperatures are obtained in Table 2. The parameters of the base and subgrade were the same as those in Reference [51].

3.2.3. UMAT Subroutine. Based on the secondary development platform provided by ABAQUS, the UMAT user subroutine was compiled. Through interface parameters and the ABAQUS main program data exchange and call, the Burgers model considering creep parameter damage was realized, as described in Figure 4. The key steps of introducing damage were as follows:

(1) Based on the existing seven variables of the revised Burgers model, the damage parameters A and B were defined as PARAM (8) and PARAM (9), respectively. The damage time was defined as PARAM (10).

(2) In the transient elastic analysis step, the material parameter E_1, which represents the elasticity, was introduced into the damage equation through the following statements: "E_1 = PARAM (4) ∗ (ONE-PARAM (8) ∗ ((TIME (1) + PARAM (10)) ∗∗ PARAM (9)))."

(3) In the viscosity analysis step, the material parameters E_2, A, and η_2 at any time are introduced into the damage equation by the following statements:

"E_2 = PARAM (4) ∗ (ONE-PARAM(8) ∗ ((TIME(1) + PARAM(10)) ∗∗ PARAM(9)))

η_2 = PARAM (5) ∗ ONE-PARAM (8) ∗ ((TIME (1) + PARAM (10)) ∗∗ PARAM (9)))

A = PARAM (6) ∗ (ONE-PARAM (8) ∗ ((TIME (1) + PARAM (10)) ∗∗ PARAM (9)))".

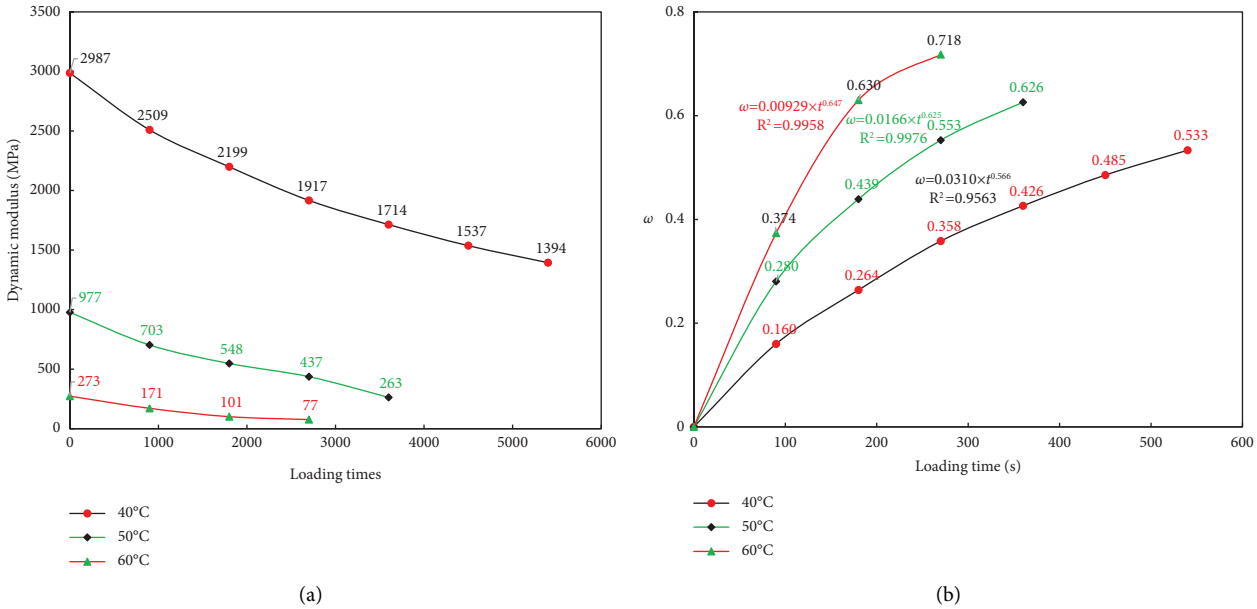

Figure 5: Repeated loading test results: (a) dynamic modulus; (b) ω.

Table 2: Creep parameters of asphalt mixtures at different temperatures.

Temperature (°C)	E_2 (MPa)	η_2 (MPa•s)	A (MPa)	B (s^{-1})	E_1 (MPa)	a	b
40	79.150	4523.705	102.143	0.001486	1634	0.00041	0.656
50	67.539	3041.990	77.578	0.001905	283	0.00046	0.641
60	56.372	1375.671	66.589	0.003568	117	0.00183	0.511

The FE model sets the pavement width and structural layer thickness according to the actual pavement size. The model size was 8 m × 6 m × 3.74 m. The load was arranged in the middle of the model's top surface. The principle of thickening to thinning from the surface layer and loading area to the distal end was adopted in grid division with the CPE8R plane strain element type. Transverse constraints were arranged on the left and right sides by selecting XSYMM ($U1 = UR2 = UR3 = 0$). Vertical constraints were arranged at the bottom by selecting ZASYMM ($U1 = U2 = UR3 = 0$).

3.3. Rutting Estimation

3.3.1. Normalization of the Rutting Deformation Curve. To eliminate the influence of different temperatures on rutting deformation and explore the rutting deformation law under uniform conditions, the rutting deformation curve under different loading conditions was transformed into the rutting curve under standard conditions using numerical simulation.

(1) The same standard loading conditions were formulated as the APT scheme.

(2) The FE simulation divided the loading cycle into several subintervals under different test conditions. The rutting prediction model was used to calculate the rutting deformation under standard conditions and each subinterval condition with an accumulated axle load of 100,000 times.

(3) The rutting correction coefficient in each interval was obtained according to the proportional relation between the nonstandard condition and the rutting deformation under the standard condition. The rutting deformation in each subinterval was multiplied by the corresponding correction coefficient to calculate the standard deformation in this subinterval. The modified rut curve was obtained by accumulating the rutting deformation in each subinterval.

3.3.2. Conversion of Axle Load Action Times Based on the Rutting Equivalent. The Hu-Ning (G2) highway with the same structures as the tested road was an example of creating the corresponding relationship between the action times $ESAL_0$ of loading weight in the tested road and the action times $ESAL_s$ of axle load in this highway. The transverse distribution law of the wheel track on this highway was investigated to obtain the transverse distribution coefficient, as presented in Figure 6.

Then, axle load conversion was conducted according to equation (8) through the lane coefficient and wheel track transverse distribution coefficient based on the rutting equivalent principle.

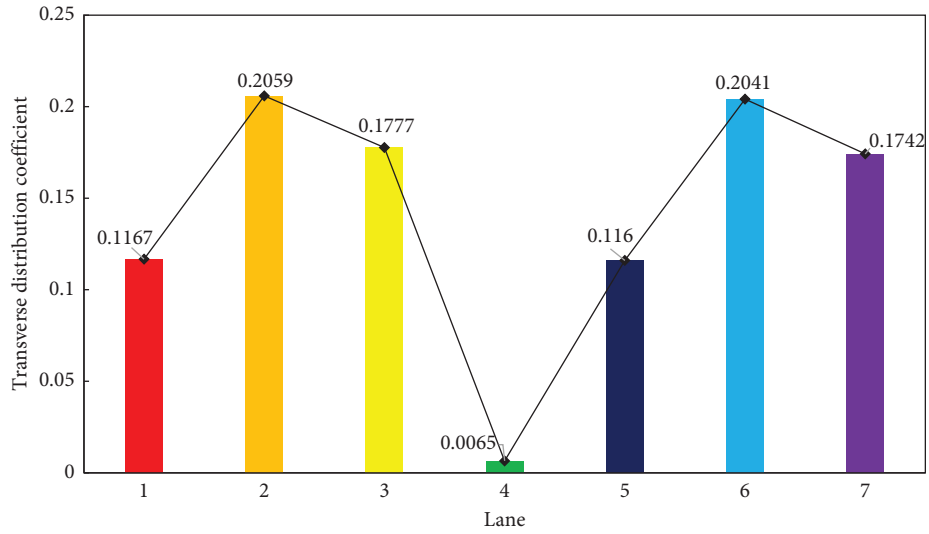

Figure 6: Lane transverse distribution coefficient of the Hu-Ning Highway.

$$N_e = \frac{N_m}{\eta \times \varphi}, \tag{8}$$

where N_e and N_m are the axle load coefficients considering the lateral distribution and APT, respectively. η is the coefficient of lanes, which was taken at 0.7 for the one direction with two lanes. φ is the lane transverse distribution coefficient, taken at 0.2059 according to the maximum value in Figure 6. To solve the problem of speed mismatch, k_v was defined as the speed conversion coefficient between the actual speed and loading speed in (9).

$$k_v = \frac{R_{vr}}{R_{v22}}, \tag{9}$$

where R_{v22} is the rutting deformation under APT, which was taken at 11.72 mm according to Figure 7. R_{vr} is the rutting deformation of the actual speed, which was calculated by the FE model. Combined with equations (8) and (9), the actual cumulative action times N_r of the axle load based on the rutting equivalent principle were obtained in (10).

$$N_r = \frac{N_e}{k_v} = \frac{N_m}{\eta \times \varphi \times k_v}. \tag{10}$$

3.3.3. Rutting Estimation of Typical Situation

(1) Different Temperature Fields. Temperature has a significant effect on the properties of asphalt and the asphalt mixture [52–54]. The temperature field data collected in the test road are divided into the following four categories in Table 3 according to the seasonal characteristics and temperature values. In the simulation, the specified load was 100 kN for the standard axle load, the driving speed was 60 km/h, and the cumulative number of axle load actions was one million times.

(2) Heavy Axle Loads. The working conditions with axle loads of 100 kN, 120 kN, and 150 kN were calculated to study the influence of heavy axle loads on rutting deformation. In the simulation, the specified temperature was based on the typical temperature field in July, the driving speed was 60 km/h, and the action time of the axle load was 500,000. Load transformation parameters in the prediction model are shown in Table 4 [51, 55].

4. Results and Discussions

4.1. Evolution Rules of Rutting

4.1.1. Morphometric Analysis of Rutting. The rutting morphology of the four test sections changes with loading times, as shown in Figure 8. Several points were evident from the results. Under repeated loading action, the rutting of each section was in the state of "W," that is, the two sides of the wheel track belt appeared to bulge. The phenomenon of bulge accompanied two sides of the wheel track. The gap between the two loading wheels was squeezed and convex. These results are in line with previous studies [45, 56]. There was almost no deformation when the loading times were less than 20,000. When it was greater than 21,000, a significant bulge appeared on both sides of the wheel track. The depression depth and bulge height increased synchronously with loading times. When it increased to 90,000, the rutting was mainly depression. The rutting section began to show a slight bulge when it increased further. The rutting deformation curves of each section were distributed within a transverse distance of 1200 mm. Two loading wheels were located at horizontal coordinates of 300 mm to 550 mm and 650 mm to 900 mm. The lateral distance of the rutting depression on both sides was approximately 270 mm. The lateral distances of the middle and both sides of the bulge were approximately 60 mm and 300 mm, respectively. The rutting deformation of different sections was slightly different, among which the rutting of Section 2 was the smallest, and the other three were the same. This was because Section 3 was just above the buried position of some sensors on the asphalt surface, which affected the rutting deformation.

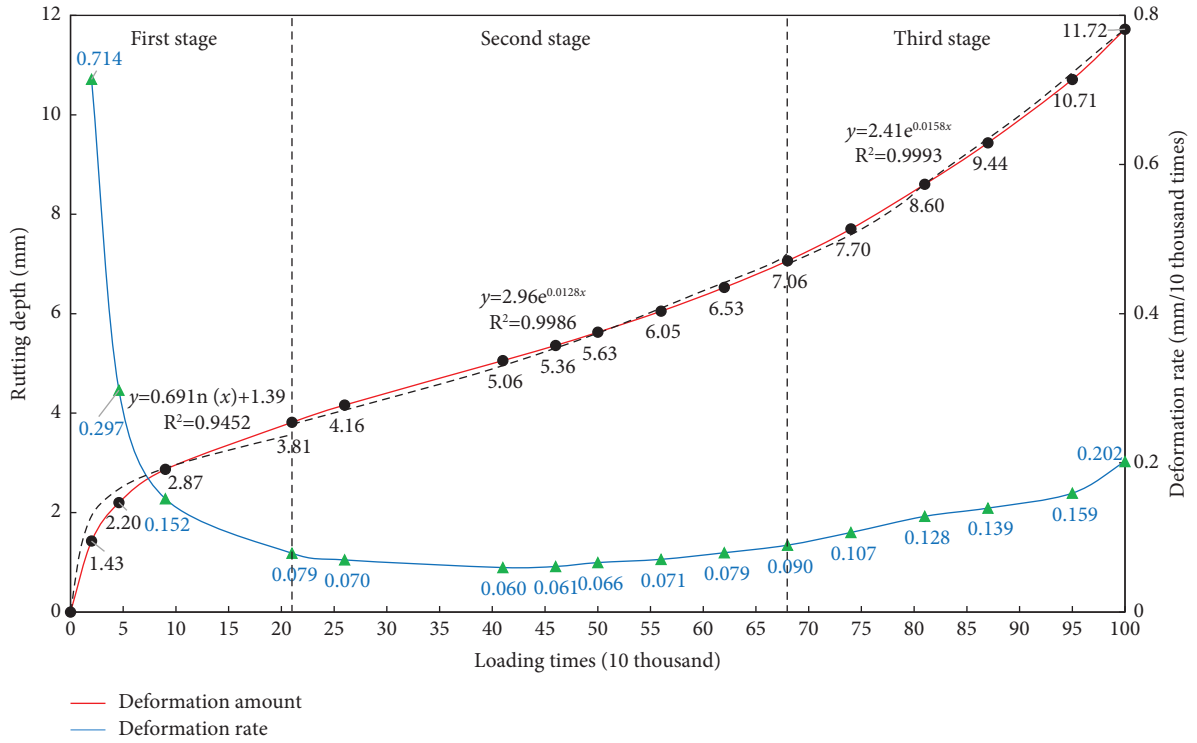

Figure 7: Rutting deformation curve after modification.

Table 3: Division of the temperature field with different seasons and months.

Season	Representative month	Temperature field
Early spring or late autumn	March, April, October	10°C to 40°C
Late spring or early autumn	May, June, September	20°C to 50°C
Summer	July, August	30°C to 60°C
Winter	December	5°C to 25°C

Table 4: Load parameters under various axle loads.

Axle load (kN)	100	150	200
Single action time of axle load (s)	0.01152	0.01383	0.01728
Single action time of axle load (s)	5760	6912	8640
Tyre action area (cm^2)	18.6 × 19.2	18.6 × 23.0	18.6 × 28.8

Figure 9 shows the structural layer thickness after repeated loading. The left depression was taken as an example based on the thickness of the shoulder: the contribution rate of deformation of the upper layer to the whole was $(4.3 - 3.9)/(17.2 - 15.8) = 28.57\%$ and that of the middle surface layer and the lower surface layer were 28.57% and 42.86%, respectively.

4.1.2. Analysis of Rutting Development. Figure 10 presents the relationship between the rutting deformation of four sections with loading times. In general, the maximum rutting deformation of each section increased with loading times. In the loading process, within 170,000 times, the average temperature was 20°C. The rutting development rate was relatively slow. When the loading time reached 170,000, the average rutting depth of each section was approximately 2.889 mm, with a growth rate of 0.169 mm per 10,000 times. During the 170,000 to 260,000 loading times, the temperatures were 40°C and 35°C, respectively. The rutting development rate increased significantly, resulting in rapid accumulation. When the loading time reaches 260,000, the average rutting depth of each section reaches 5.562 mm, with a deformation rate of 0.297 mm per 10,000 times. During the 260,000 to 410,000 loading times, the average temperature was between 18°C and 26°C. The rutting development rate slowed down. When it reached 410,000, the average rutting depth was 5.743 mm, with a deformation rate of 0.012 mm per 10,000 times. During the 410,000 to 740,000 loading times, the average temperature was between 32°C and 36°C.

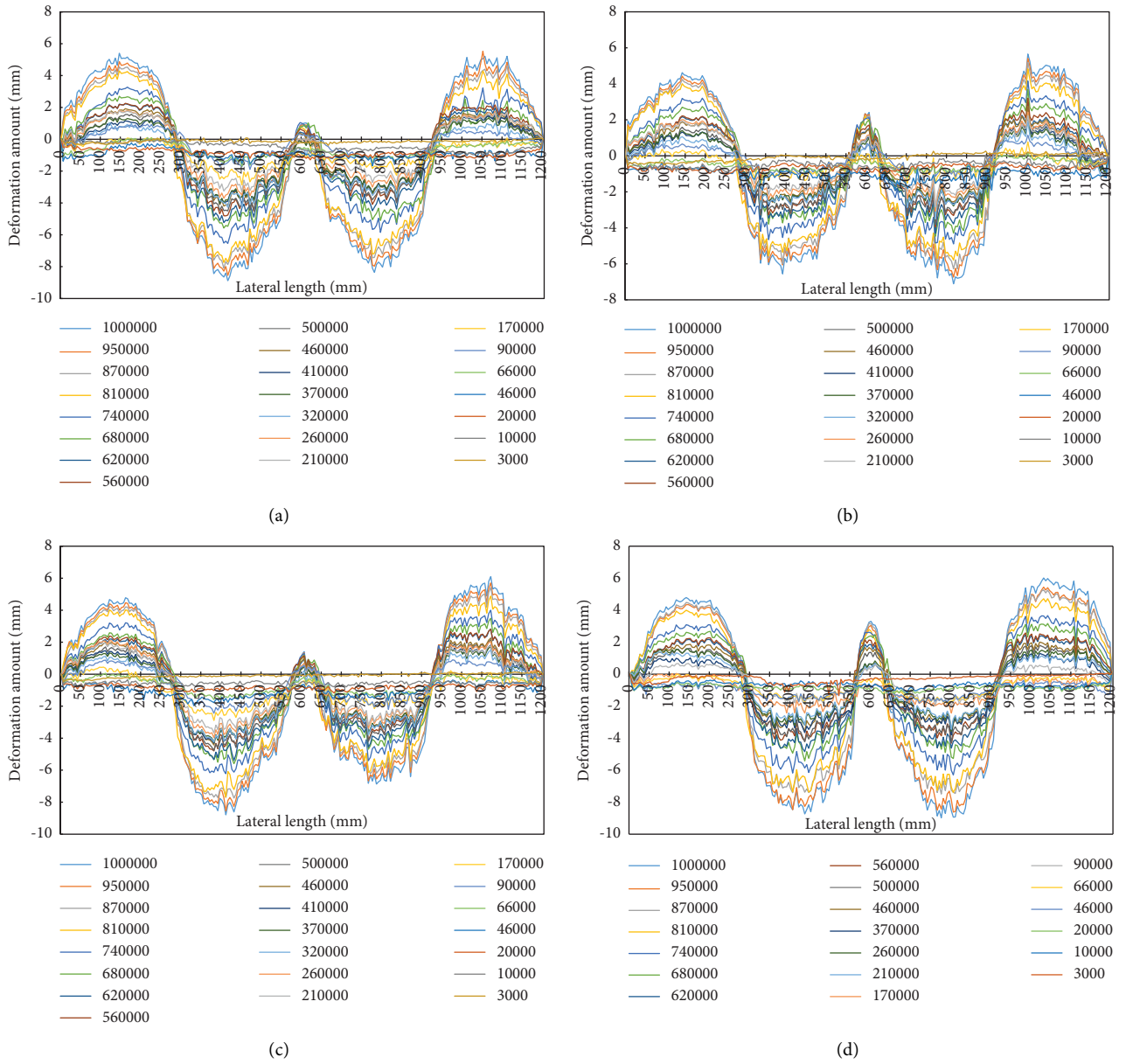

Figure 8: Change curve of rutting deformation with loading times: (a–d) Section 1 to Section 4.

The rutting development rate increased, and the rutting depth increased stably. When it reached 740,000, the average rutting depth was 9.763 mm, with a deformation rate of 0.122 mm per 10,000 times. During the 740,000 to 1030,000 loading times, the average temperature was approximately 45°C. The rutting rate increased further. When it reached 1030,000, the average rutting depth was 14.473 mm, with a deformation rate of 0.162 mm per 10,000 times. These rules of rutting deformation are consistent with the previous works [57, 58].

From this, the rutting deformation rate is positively correlated with the temperature. Therefore, to further study the influence of loading under different temperature conditions on the maximum rutting deformation, the loading times and the rutting deformation and proportion, respectively, under different temperature conditions are investigated in Table 5. The contribution of loading to rutting deformation was small at low temperatures. However, when the test road was under high-temperature conditions, rutting increased significantly with 360,000 loading times, producing a rutting of 7.9 mm and contributing a rate of 56.04%. This indicates that temperature plays a vital role in the influence of the rutting development rate.

4.1.3. Mechanism Analysis of Rutting Deformation. Figure 11 describes the four sections' average rutting deformation area-loading times relationship curve. Generally,

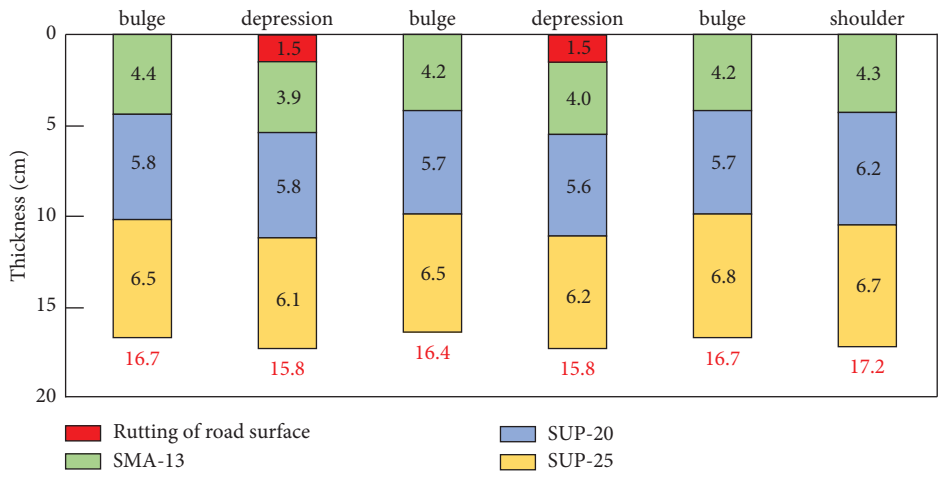

Figure 9: Schematic diagram of the core sample thickness of the tested sections.

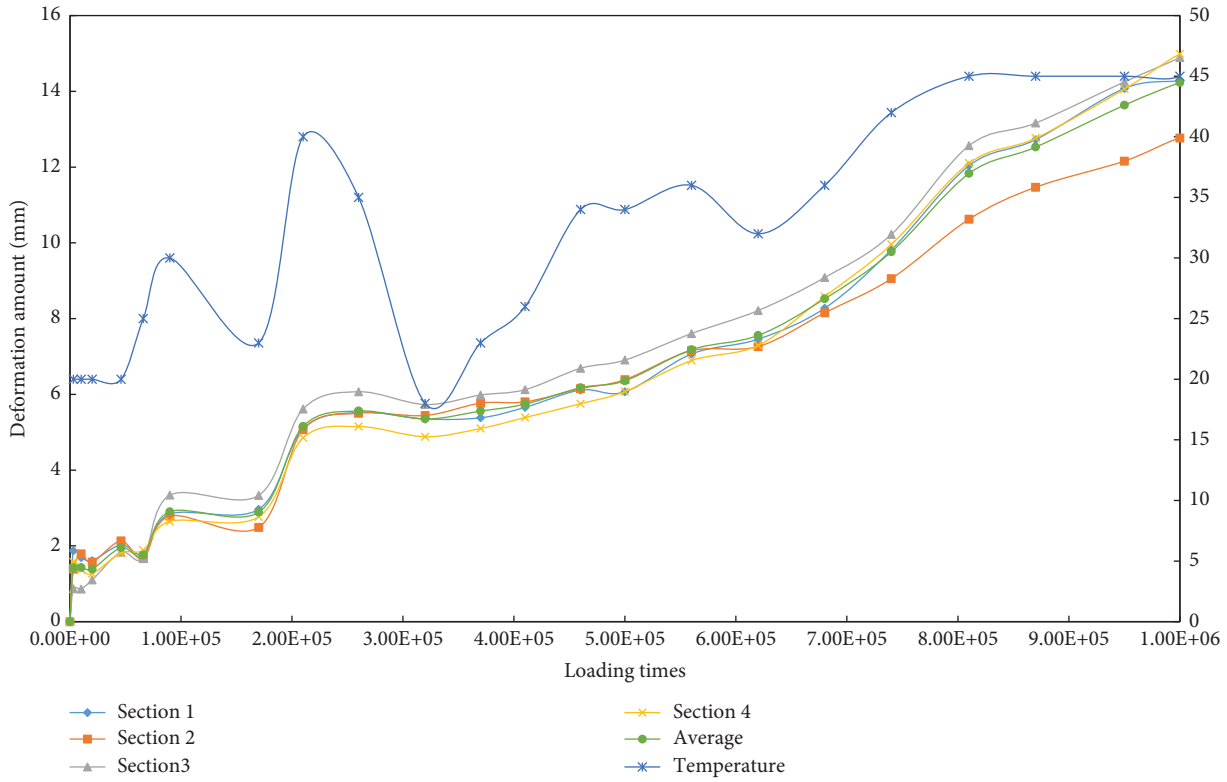

Figure 10: Change curve of rutting deformation of each section with loading times and temperature at the bottom of the middle surface layer.

Table 5: Loading times and rutting ratio under different temperature conditions.

Temperature conditions	Loading times (ten thousand)	Rutting deformation amount (mm)	Ration
Low temperature (18°C to 28°C)	29.6	1.9	13.51
Middle temperature (28°C to 37°C)	34.4	4.3	30.45
High temperature (37°C to 45°C)	36	7.9	56.04

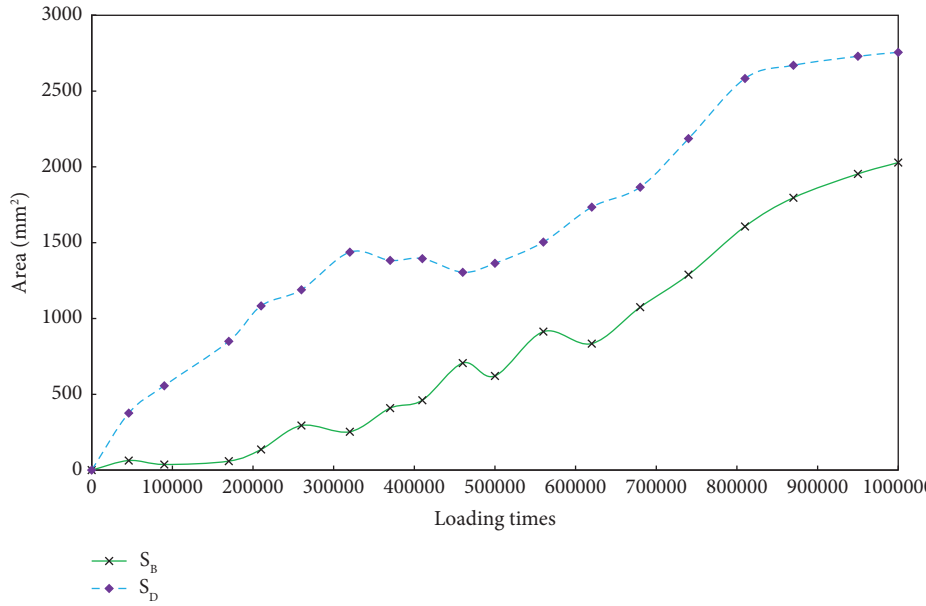

Figure 11: Relationship curve of average rutting deformation area and loading times.

each section's S_B and S_D increased with the loading times. It is worth noting that the lateral bulge of the track belt at each section began to occur gradually after 210,000 loading times.

Figure 12 demonstrates the change law of K_R. After 210,000 loading times, rutting deformation entered the first stable period (K_R increased rapidly), indicating that compaction and flow rutting cooccurred at this stage, but compaction ruts were still the main ruts at this time. After loading 680,000 times, rutting deformation entered the second stable period (K_R increased slowly), indicating that the rutting form began to transition from compaction rut to shear flow rutting. This is because, in addition to the continuous increase in compaction deformation, the shear strength of the underlying layer of materials at high temperatures is insufficient due to the increase in loading temperature, lateral flow of the asphalt mixture occurs, shear flow deformation begins to occur, and the two kinds of deformation increase simultaneously. After loading 810,000 times, rutting deformation development entered a new stage (K_R increased slowly). The S_D tends to be stable, indicating that the rutting development form was dominated by shear flow deformation, which agrees with Ling's results [45]. These analysis results are summarized in Table 6.

4.2. Experimental Results of Parameters of Asphalt Mixture

4.2.1. Results of Dynamic Modulus Test. After one million loading times, the average test value of the dynamic modulus was 62% of that before loading, indicating that the material parameters of the asphalt surface obviously decay with the loading process.

4.2.2. Results of Repeated Loading Test. The repeated loading test and fitted results are presented in Figure 5. The asphalt mixture's residual dynamic modulus decreased with the loading times. When the test temperature was 40°C, the dynamic modulus decreased to 46% of the initial values after 5,400 loading times. After that, the dynamic modulus attenuated 50% and 48% of the initial values after 2,700 loading times at 50°C and 60°C, respectively. This is because the stiffness modulus of asphalt binder decreases gradually with an increase in temperature, which weakens its resilience under stress.

4.2.3. Results of Dynamic Creep Test. The comparison of the dynamic creep curve test results at different temperatures is shown in Figure 13. Apparently, the deformation development rate of asphalt mixtures increased rapidly with increasing temperature. When the specimens were loaded 906, 3,309, and 14,481 times at 40°C, 50°C, and 60°C, respectively, the rutting deformation reached 15 mm. This once again confirmed the serious influence of temperature on rutting deformation: with increasing loading times, the difference in rutting deformation under different loading temperatures was greater.

4.3. Numerical Simulation Results of Rutting Estimation. After loading the FE model a million times, the final deformation pattern of rutting is shown in Figure 14. The final rutting deformation was 13.56 mm, with an error rate of 7.9% from the measured results (14.233 mm). The simulated and measured values of rutting deformation had the same

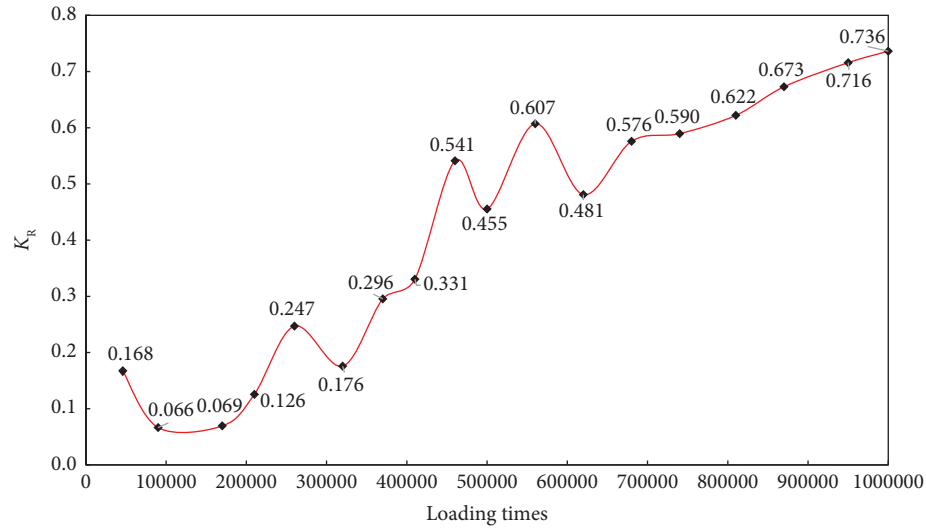

Figure 12: Change curve of K_R with loading times.

tendency to change with loading times. The error within 10% of the rutting prediction model was within the acceptable range, which can be used to guide the rutting prediction of asphalt pavement with a semirigid base. These results confirm the validation of the MEPDG method for rutting prediction in Tian's study [59].

4.3.1. Normalization Results of the Rutting Deformation Curve. Figure 14 presents the modified rutting deformation curve. The overall development trend was consistent with the results in Figure 12 and Table 5. The causes of rutting deformation in different loading stages are summarized as follows: in the first stage (0 to 210,000 loading times), the slurry composed of asphalt, mineral powder, and semifluid asphalt is squeezed into the ore gap in the process of high-temperature rolling. Insufficient vertical bearing capacity of the road surface caused the material's volume and porosity to decrease, causing compaction and rutting deformation. In the second stage (210,000 to 680,000 loading times), asphalt and asphalt mortar will flow freely with the asphalt mixture in addition to partially filling the mixture void under loads. As a result, the insufficient shear resistance of materials began to produce flow deformation. Compaction and flow deformation increased simultaneously. Although rutting deformation was still dominated by compaction deformation, the growth rate of shear deformation was higher than that of compaction deformation, thus showing the stable growth of rutting deformation. Third stage (680,000 to one million loading times): with further damage to the material, the shear resistance of asphalt mixtures decreased further. Asphalt and mortar flow to the enrichment region, resulting in the loss of stability of the asphalt mixture structure. Thus, the compaction deformation gradually stagnated while the lateral shear flow deformation occupied the dominant position and the deformation rate increased rapidly. Rutting deformation was dominated by flow deformation. The above results confirm the theory of Lv et al. [8] that rutting deformation of asphalt pavement could be divided into three stages.

4.3.2. Action Time of Axle Load on Investigated Highway. Table 7 shows the equivalent axle load action times on the Hu-Ning highway. The cumulative action time of the standard axle load obtained by simulation was 36.71 million when the rutting deformation was 14.23 mm. According to the Hu-Ning highway survey data, the action time was 38.5 million times, with a rutting deformation of 15 mm. The comparison shows a minor error between the predicted and the actual data. Thus, the conversion method of axle load action times based on rutting equivalence proves effective. Besides, during the actual service process, for typical pavement structures, when the number of axle load actions is more than 25 million, the rutting deformation enters the third stage of accelerated failure. The results of this work are closer to the real situation compared to Li's results [60]. Therefore, this typical pavement structure needs to take the necessary maintenance measures to treat rutting damage at this time.

4.3.3. Results of Rutting Estimation under Different Working Conditions. Figure 15(a) shows the results of rutting estimation under different temperature fields. Obviously, rutting deformation and its rate increased with increasing temperature. Under the temperature field in summer, the rutting deformation curve entered the third stage after accumulating one million loading times with a rutting deformation of 4.24 mm. In winter, the rutting deformation was only 0.88 mm, which was 20.7% of the rutting deformation in summer. This relationship between rutting deformation and the temperature field is consistent with Dong's results [61]. Figure 15(b) displays the results of

Table 6: Rutting deformation law with loading times.

Loading times (ten thousand)	Compaction speed (mm^2/ten thousand)	Bulge speed (mm^2/ten thousand)	K_R	Rutting forms
0 to 21	51.57	6.48	<0.167	Compaction rutting
21 to 68	16.67	19.97	0.125 to 0.575	Compacting rutting was the main, flow rutting was supplementary
68 to 81	55.16	40.95	0.575 to 0.622	Both were equivalent
81 to 100	9.07	22.21	0.622 to 0.736	Flow rutting

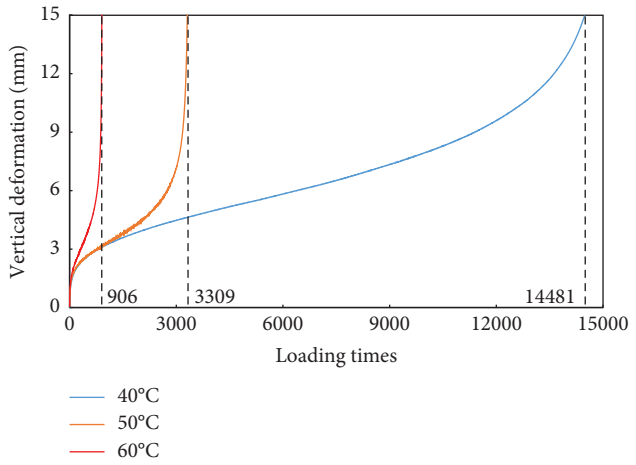

Figure 13: Dynamic creep test curves at different temperatures.

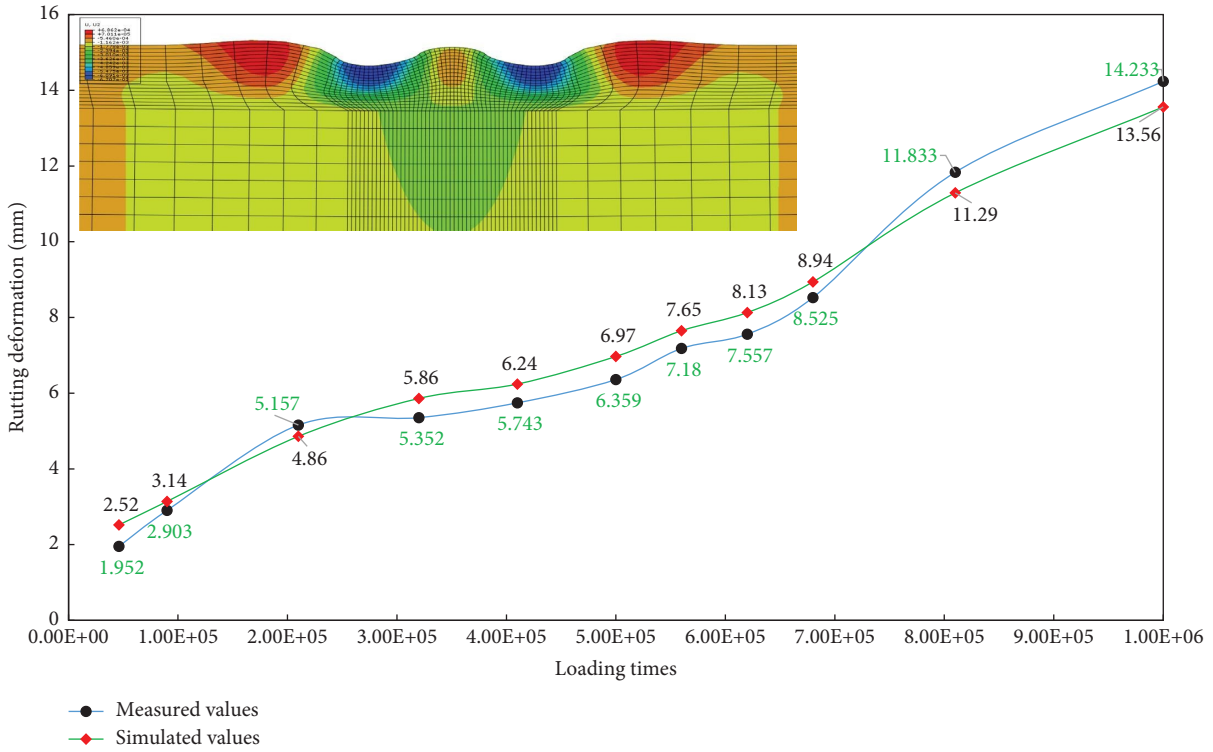

Figure 14: Comparison of simulated and measured values of rutting deformation.

Table 7: Number of equivalent axle load actions on the actual road.

$ESAL_0$ (ten thousand)	Actual rutting deformation (mm)	Modified rutting deformation (mm)	$ESAL_s$ (ten thousand)
2	1.43	1.43	73.42
4.6	1.95	2.20	168.87
9	2.90	2.87	330.39
21	5.16	3.81	770.91
26	5.56	4.16	954.46
41	5.74	5.06	1505.11
46	6.18	5.36	1688.66
50	6.36	5.63	1835.50

Table 7: Continued.

$ESAL_0$ (ten thousand)	Actual rutting deformation (mm)	Modified rutting deformation (mm)	$ESAL_s$ (ten thousand)
56	7.18	6.05	2055.76
62	7.56	6.53	2276.02
68	8.56	7.06	2496.28
74	9.76	7.70	2716.54
81	11.83	8.60	2973.51
87	12.53	9.44	3193.77
95	13.64	10.71	3487.45
100	14.23	11.72	3671.00

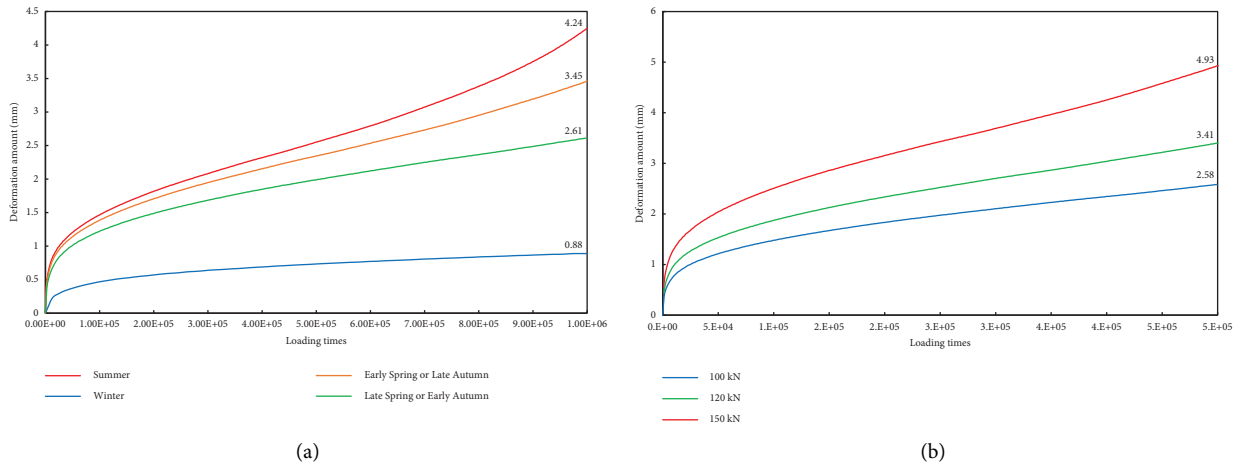

(a) (b)

Figure 15: Prediction of rutting deformation under different working conditions: (a) different temperature fields; (b) different heavy axle loads.

rutting estimation under different heavy axle loads. The figure shows that the pavement deformation increased with increasing load under the same axle loads. After 500,000 loading times, rutting deformation increased by 90.7% under a 50% overload in the high-temperature season. Therefore, overloaded vehicles should be strictly controlled in actual road service, especially in high-temperature periods.

5. Conclusions and Perspectives

This research analyzed the rutting development and evolution rules of asphalt pavement with semirigid base-based full-scale APT. The FE model for rutting prediction was established, verified, and applied. Several conclusions are drawn below:

(1) High temperatures and heavy axle loads greatly influence rutting development. The high-temperature loading occurred 360,000 times in the loading test, contributing 56.04% to the rutting development. FE simulation results showed that the rutting deformation increased by 90.7% under 50% overload in the high-temperature season.

(2) A Burgers model considering the damaging effect of creep parameters was proposed as a constitutive equation of the rutting prediction model based on the monitoring data and laboratory values. The simulated results were in good agreement with the measured results, with an error of 7.9% compared to the APT data.

(3) K_R was proposed as the index to define the rutting deformation mechanism. It was concluded from the field detection data and simulated rutting curve that the rutting development of asphalt pavement is a transition process from compaction rutting to flow rutting. $K_R = 0.1$ and $K_R = 0.5$ are the critical points at which the compacting rutting and the flow rutting begin, respectively.

(4) The relationship between $ESAL_0$ and $ESAL_s$ was established based on the rutting equivalence principle. For the typical pavement structures in Jiangsu, 7.7 million and 25 million are the demarcation points of the actual rutting deformation curves of the first, second, and third stages, respectively.

The conclusions from this study have important implications for rutting prediction and maintenance decisions on asphalt pavement. However, the limitation of this work is that the asphalt surface layer is simplified as a whole structure layer, and the structure layer always has complete interlayer continuity in the FE model. Accurate prediction of rutting deformation continues to be a challenge. Future work should focus on achieving more reliable rutting

predictions through several key points: acquisition of more measured data, establishment of a more precise FE element model, etc.

Data Availability

The data supporting the findings of this study are available from the corresponding author upon reasonable request.

Conflicts of Interest

The authors declare that they have no conflicts of interest.

Acknowledgments

This work was supported by the Scientific Research Foundation of Graduate School of Southeast University (grant no. YBPY2164).

References

[1] Z. Liu, X. Y. Gu, W. X. Wu, X. Y. Zou, Q. Dong, and L. T. Wang, "GPR-based detection of internal cracks in asphalt pavement: a combination method of DeepAugment data and object detection," *Measurement*, vol. 197, Article ID 111281, 2022.

[2] J. Huyan, T. Ma, W. Li, H. Yang, and Z. Xu, "Pixelwise asphalt concrete pavement crack detection via deep learning-based semantic segmentation method," *Structural Control and Health Monitoring*, vol. 29, no. 8, 2022.

[3] Z. Liu, J. K. W. Yeoh, X. Gu et al., "Automatic pixel-level detection of vertical cracks in asphalt pavement based on GPR investigation and improved mask R-CNN," *Automation in Construction*, vol. 146, Article ID 104689, 2023.

[4] D. Wang, Z. Liu, X. Gu, W. Wu, Y. Chen, and L. Wang, "Automatic detection of pothole distress in asphalt pavement using improved convolutional neural networks," *Remote Sensing*, vol. 14, no. 16, p. 3892, 2022.

[5] Z. Xu, Q. Zhou, G. Chen, Y. Wang, X. Yang, and Z. Liu, "An effectiveness study of spc control charts on the quality control for construction in asphalt pavement," in *Proceedings of the IOP Conference Series: Earth and Environmental Science*, June 2021, Article ID 012115.

[6] Z. Liu, X. Gu, Y. Chen, and Y. Chen, "System architecture and key technologies for the whole life cycle of smart road," *Journal of Physics: Conference Series*, vol. 1972, no. 1, Article ID 012105, 2021.

[7] C. Q. Yan, Y. Zhang, and H. U. Bahia, "Predicting rutting performance of asphalt mixture from binder properties and mixture design variables," *Road Materials and Pavement Design*, vol. 23, no. 1, pp. 62–79, 2022.

[8] J. X. Lv and X. Y. Zhang, "Prediction models of shear parameters and dynamic creep instability for asphalt mixture under different high temperatures," *Polymers*, vol. 13, no. 15, p. 2542, 2021.

[9] Z. Liu, X. Gu, J. Chen, D. Wang, Y. Chen, and L. Wang, "Automatic recognition of pavement cracks from combined GPR B-scan and C-scan images using multiscale feature fusion deep neural networks," *Automation in Construction*, vol. 146, Article ID 104698, 2023.

[10] Z. Liu, X. Gu, H. Yang, L. Wang, Y. Chen, and D. Wang, "Novel YOLOv3 model with structure and hyperparameter optimization for detection of pavement concealed cracks in GPR images," *IEEE Transactions on Intelligent Transportation Systems*, vol. 23, no. 11, pp. 22258–22268, 2022.

[11] Z. Liu, X. Y. Gu, and Q. Dong, "Multi-scale 3D display of the internal quality of the pavement based on BIM," in *Proceedings of the 19th COTA International Conference of Transportation Professionals (CICTP) - Transportation in China 2025*, pp. 4265–4273, Nanjing, China, July 2019.

[12] H. Ren, X. Gu, and Z. Liu, "Analysis of mechanical responses for semi-rigid base asphalt pavement based on mls66 accelerated loading test," in *Proceedings of the CICTP 2021*, pp. 732–742, Xi'an, China, December 2021.

[13] X. Gu, J. Lu, X. Zhang, and X. Zou, "Prediction models of creep instability points for asphalt mixtures at high temperature and parameters effects on model," *Journal of Southeast University. Natural Science Edition*, vol. 47, no. 5, pp. 1013–1019, 2017.

[14] Y. Tian, J. Lee, T. Nantung, and J. E. Haddock, "Development of a mid-depth profile monitoring system for accelerated pavement testing," *Construction and Building Materials*, vol. 140, pp. 1–9, 2017.

[15] P. J. V. D. Loo, "Practical approach to the prediction of rutting in asphalt pavements: the shell method," *Transportation Research Record*, vol. 616, 1976.

[16] A. Wijeratne and M. Sargious, "Prediction of rutting in virgin and recycled asphalt mixtures for pavements using triaxial tests," *Association of Asphalt Paving Technologists Proc*, vol. 56, 1987.

[17] L. Li, Y. Zhang, and Y. Zhang, "Prediction of fatigue performance of asphalt pavement considering interlayer contact behavior," *Journal of Dalian University of Technolgy*, vol. 61, no. 3, pp. 280–287, 2021.

[18] H. I. Shami, J. S. Lai, J. A. D'Angelo, and T. P. Harman, "B. transportat res board; transportat res board; transportat res, development of temperature-effect model for predicting rutting of asphalt mixtures using georgia loaded wheel tester," in *Proceedings of the 76th Annual Meeting of the Transportation-Research-Board*, pp. 17–22, Washington, DC, USA, 1997.

[19] A. R. Archilla and S. Madanat, "Development of a pavement rutting model from experimental data," *Journal of Transportation Engineering*, vol. 126, no. 4, pp. 291–299, 2000.

[20] L. U. Zhenglan and S. U. N. Lijun, "Research on rutting prediction of asphalt pavement," *Journal of Tongji University. Natural Science*, vol. 35, no. 11, pp. 1476–1480, 2007.

[21] K. Hoegh, L. Khazanovich, and M. Jensen, "Local calibration of mechanistic-empirical pavement design guide rutting model Minnesota road research project test sections," *Transportation Research Record*, vol. 2180, no. 1, pp. 130–141, 2010.

[22] N. Solatifar, A. Kavussi, M. Abbasghorbani, and S. W. Katicha, "Development of dynamic modulus master curves of in-service asphalt layers using MEPDG models," *Road Materials and Pavement Design*, vol. 20, no. 1, pp. 225–243, 2019.

[23] E. J. Gulfam, X.-X. Yuan, and M. Shehata, "Development of regression equations for local calibration of rutting and IRI as predicted by the MEPDG models for flexible pavements using Ontario's long-term PMS data," *International Journal of Pavement Engineering*, vol. 17, no. 2, pp. 166–175, 2016.

[24] H. F. H. Abdelfattah, H. Baaj, and H. J. Kadhim, "Calibration of MEPDG permanent deformation models using Hamburg Wheel Rut Tester and field data," *International Journal of Pavement Engineering*, vol. 23, no. 12, pp. 4174–4189, 2021.

[25] J. W. Zhu, L. J. Sun, Y. Wang, H. Li, and L. P. Liu, "Development and calibration of shear-based rutting model for asphalt concrete layers," *International Journal of Pavement Engineering*, vol. 18, no. 10, pp. 937–944, 2017.

[26] Y. Deng, X. Luo, Y. Zhang et al., "Determination of flexible pavement deterioration conditions using Long-Term Pavement Performance database and artificial intelligence-based finite element model updating," *Structural Control and Health Monitoring*, vol. 28, no. 2, 2021.

[27] J. W. Jiang, F. J. Ni, L. Gao, and S. X. Lou, "Developing an optional multiple repeated load test to evaluate permanent deformation of asphalt mixtures based on axle load spectrum," *Construction and Building Materials*, vol. 122, pp. 254–263, 2016.

[28] B. Cui, X. Gu, D. Hu, and Q. Dong, "A multiphysics evaluation of the rejuvenator effects on aged asphalt using molecular dynamics simulations," *Journal of Cleaner Production*, vol. 259, Article ID 120629, 2020.

[29] H. L. Yang, S. J. Wang, Y. H. Miao, L. B. Wang, and F. Y. Sun, "Effects of accelerated loading on the stress response and rutting of pavements," *Journal of Zhejiang University - Science A*, vol. 22, no. 7, pp. 514–527, 2021.

[30] Y. Tan, Z. Liang, H. Xu, and C. Xing, "Research on rutting deformation monitoring method based on intelligent aggregate," *IEEE Transactions on Intelligent Transportation Systems*, vol. 23, no. 11, pp. 22116–22126, 2022.

[31] X. P. Ji, N. X. Zheng, S. S. Niu, S. T. Meng, and Q. L. Xu, "Development of a rutting prediction model for asphalt pavements with the use of an accelerated loading facility," *Road Materials and Pavement Design*, vol. 17, no. 1, pp. 15–31, 2016.

[32] J. Füssl, W. Kluger-Eigl, and R. Blab, "Mechanical performance of pavement structures with paving slabs - Part I: full-scale accelerated tests as validation for a numerical simulation tool," *Engineering Structures*, vol. 98, pp. 212–220, 2015.

[33] R. Blab, W. Kluger-Eigl, J. Füssl, M. Arraigada, and B. Hofko, "Accelerated pavement testing on slab and block pavements using the new mobile load simulator MLS10," in *Proceedings of the 4th international conference on accelerated pavement testing*, Davis, CA, USA, October 2012.

[34] X. P. Ji, N. X. Zheng, Y. Q. Hou, and S. S. Niu, "Application of asphalt mixture shear strength to evaluate pavement rutting with accelerated loading facility (ALF)," *Construction and Building Materials*, vol. 41, pp. 1–8, 2013.

[35] D. Jansen, B. Wacker, and L. Pinkofsky, "Full-scale accelerated pavement testing with the MLS30 on innovative testing infrastructures," *International Journal of Pavement Engineering*, vol. 19, no. 5, pp. 456–465, 2018.

[36] F. Zhou and T. Scullion, "Vesys5 rutting model calibrations with local accelerated pavement test data and associated implementation," Case Studies, Texas, TX, USA, FHWA/TX-03/9-1502-01-2, 2002.

[37] F. Hugo, A. Martin, B. Choubane et al., "Significant findings from full-scale accelerated pavement testing," *Transportation Research Board*, vol. 325, 2004.

[38] J. Fussl, W. Kluger-Eigl, L. Eberhardsteiner, and R. Blab, "Mechanical performance of pavement structures with paving slabs - Part II: numerical simulation tool validated by means of full-scale accelerated tests," *Engineering Structures*, vol. 98, pp. 221–229, 2015.

[39] J. M. Ling, F. L. Wei, H. D. Zhao, Y. Tian, B. Y. Han, and Z. A. Chen, "Analysis of airfield composite pavement responses using full-scale accelerated pavement testing and finite element method," *Construction and Building Materials*, vol. 212, pp. 596–606, 2019.

[40] Y. C. Huang, L. B. Wang, and H. C. Xiong, "Evaluation of pavement response and performance under different scales of APT facilities," *Road Materials and Pavement Design*, vol. 18, no. sup3, pp. 159–169, 2017.

[41] Z. Liu and X. Gu, "Performance evaluation of full-scale accelerated pavement using ndt and laboratory tests: a case study in jiangsu, china," *Case Studies in Construction Materials*, vol. 18, Article ID e02083, 2023.

[42] Z. Liu, X. Gu, and R. Hong, "Fire protection and evacuation analysis in underground interchange tunnels by integrating BIM and numerical simulation," *Fire*, vol. 6, no. 4, p. 139, 2023.

[43] L. T. Wang, X. Y. Gu, Z. Liu, W. X. Wu, and D. Y. Wang, "Automatic detection of asphalt pavement thickness: a method combining GPR images and improved Canny algorithm," *Measurement*, vol. 196, Article ID 111248, 2022.

[44] B. Cui, H. Wang, X. Gu, and D. Hu, "Study of the interdiffusion characteristics and cracking resistance of virgin-aged asphalt binders using molecular dynamics simulation," *Construction and Building Materials*, vol. 351, Article ID 128968, 2022.

[45] J. Ling, L. Ren, Y. Tian, J. Gao, and L. Man, "Analysis of airfield composite pavement rutting using full-scale accelerated pavement testing and finite element method," *Construction and Building Materials*, vol. 303, Article ID 124528, 2021.

[46] Z. Liu, X. Y. Gu, H. Ren, Z. Zhou, X. Wang, and S. Tang, "Analysis of the dynamic responses of asphalt pavement based on full-scale accelerated testing and finite element simulation," *Construction and Building Materials*, vol. 325, Article ID 136249, 2022.

[47] Z. Liu, X. Y. Gu, C. Y. Wu, H. Ren, Z. Zhou, and S. Tang, "Studies on the validity of strain sensors for pavement monitoring: a case study for a fiber Bragg grating sensor and resistive sensor," *Construction and Building Materials*, vol. 321, Article ID 126085, 2022.

[48] R. Ou, L. Luo, and K. Soga, "Brillouin scattering spectrum-based crack measurement using distributed fiber optic sensing," *Structural Health Monitoring*, vol. 21, no. 4, pp. 1345–1366, 2022.

[49] W. Liu, H. Wang, Z. Zhou, X. Xing, D. Cao, and Z. Jiang, "Optical fiber-based sensors with flexible encapsulation for pavement behavior monitoring," *Structural Control and Health Monitoring*, vol. 22, no. 2, pp. 301–313, 2015.

[50] D. Han, G. Liu, Y. Xi, and Y. Zhao, "Theoretical analysis on the measurement accuracy of embedded strain sensor in asphalt pavement dynamic response monitoring based on FEM," *Structural Control and Health Monitoring*, vol. 29, no. 12, Article ID e3140, 2022.

[51] Z. Liu, X. Y. Gu, H. Ren, X. Wang, and Q. Dong, "Three-dimensional finite element analysis for structural parameters of asphalt pavement: a combined laboratory and field accelerated testing approach," *Case Studies in Construction Materials*, vol. 17, Article ID e01221, 2022.

[52] Z. Liu, L. Sun, X. Gu et al., "Characteristics, mechanisms, and environmental LCA of WMA containing sasobit: an analysis perspective combing viscosity-temperature regression and interface bonding strength," *Journal of Cleaner Production*, vol. 391, Article ID 136255, 2023.

[53] Z. Liu, X. Gu, X. Dong, B. Cui, and D. Hu, "Mechanism and performance of graphene modified asphalt: an experimental approach combined with molecular dynamic simulations,"

Case Studies in Construction Materials, vol. 18, Article ID e01749, 2023.

[54] Z. Liu, S. Y. Wang, X. Y. Gu, Z. G. Li, Q. Dong, and B. Y. Cui, "Application of a novel EWMA-phi chart on quality control in asphalt mixtures production," *Construction and Building Materials*, vol. 323, Article ID 126264, 2022.

[55] Z. Liu, X. Gu, and H. Ren, "Rutting prediction of asphalt pavement with semi-rigid base: numerical modeling on laboratory to accelerated pavement testing," *Construction and Building Materials*, vol. 375, Article ID 130903, 2023.

[56] G. Liu, L. Chen, Z. Qian, Y. Zhang, and H. Ren, "Rutting prediction models for asphalt pavements with different base types based on RIOHTrack full-scale track," *Construction and Building Materials*, vol. 305, Article ID 124793, 2021.

[57] S. Li, M. Fan, L. Xu, W. Tian, H. Yu, and K. Xu, "Rutting performance of semi-rigid base pavement in RIOHTrack and laboratory evaluation," *Frontiers in Materials*, vol. 7, 2021.

[58] Y. Pan, G. Liu, D. Tang, D. Han, X. Li, and Y. Zhao, "A rutting-based optimum maintenance decision strategy of hot in-place recycling in semi-rigid base asphalt pavement," *Journal of Cleaner Production*, vol. 297, Article ID 126663, 2021.

[59] Y. Tian, J. Lee, T. Nantung, and J. E. Haddock, "Calibrating the mechanistic–empirical pavement design guide rutting models using accelerated pavement testing," *Transportation Research Record*, vol. 2672, no. 40, pp. 304–314, 2018.

[60] H. Li and F. Ni, "Investigation into application time of highway asphalt pavement preventive maintenance treatments," in *Proceedings of the CICTP*, pp. 938–948, Beijing, China, July 2015.

[61] N. Dong, F. Ni, L. Zhou, and X. Ma, "Comparison of the Hamburg, indirect tensile, and multi-sequenced repeated load tests for evaluation of HMA rutting resistance," *Construction and Building Materials*, vol. 216, pp. 588–598, 2019.